International Journal of Heat and Fluid Flow 118 (2026) 110207

Contents lists available at ScienceDirect

International Journal of Heat and Fluid Flow

journal homepage: www.elsevier.com/locate/ijhff

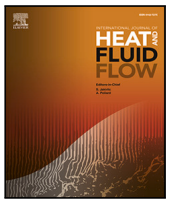

Direct numerical simulation of installation effects on airfoil noise

Ziyang Zhou [a,*], Stéphane Moreau [a], Marlène Sanjosé [b]

[a] Department of Mechanical Engineering, Université de Sherbrooke, 2500 blvd de l'Université, Sherbrooke, J1K2R1, QC, Canada
[b] Department of Aerospace Engineering, École de Technologie Supérieure, 1100 rue Notre Dame Ouest, Montréal, H3C1K3, QC, Canada

ARTICLE INFO

Keywords:
Aeroacoustics
Airfoil noise
Direct numerical simulation

ABSTRACT

To evaluate installation effects on velocity statistics and its influence on farfield noise, three Direct Numerical Simulations (DNS) have been run using the Lattice-Boltzmann Method with the PowerFLOW software on the Controlled-Diffusion (CD) airfoil at a Reynolds number of 150 000 and 8 degrees angle of attack installed in the Universite de Sherbrooke (UdeS) wind tunnel. Differences in setup between these DNS simulations are the addition of voxel refinements and turbulent trips to the simulation setup for better capturing of the jet shear layer downstream of the wind tunnel nozzle lip. Results show that the airfoil boundary layer displacement thickness, momentum thickness and shape factor are slightly increased after jet shear layer refinement due to an increase in mean angle of attack caused by a change in shear layer state. Despite these changes caused by the mixing layer state, maximum Reynolds stress magnitude near the trailing edge of the airfoil was changed by only 6%. This indicates that adjustments to the wall pressure statistics which are relevant to trailing edge noise generation was only marginal. As such, changes to boundary layer statistics had limited impact on far-field noise in the mid-frequency range in this operating state.

1. Introduction

Recent improvements in turbomachinery noise have led to a strong reduction of tonal noise in rotating machines. Broadband noise contribution is then becoming more and more important. When under clean and controlled inlet flow conditions, the main broadband noise mechanism is the sound produced at the trailing edge of blades. Any turbulence or flow disturbance born in the boundary layer of any lifting surface generates pressure fluctuations and vorticity distortions that scatter at the trailing edge and cause acoustic emissions.

Many numerical studies analyzed the flow around airfoils to isolate the trailing-edge (TE) noise mechanisms because it is a canonical flow problem to investigate TE noise in turbomachines. In the present study, the flow around a controlled diffusion (CD) airfoil in an anechoic open-jet facility is investigated. The chord based Reynolds number is 1.5×10^5 and the Mach number is 0.05, characteristic of low speed fan systems. This configuration has become a reference case study for trailing-edge noise as both aerodynamic and acoustic data have been collected experimentally and numerically. The experimental database provides hotwire measurements to characterize the incoming flow, the boundary-layer on the suction side, near and far wake and the jet shear layers (Moreau et al., 2006). Mean-pressure coefficient and wall-pressure spectra at several locations on the airfoil pressure and suction sides have also been measured (Roger and Moreau, 2004; Moreau and Roger, 2005). Far field sound and directivity spectra have been recorded in the mid-span plane of the mock-up.

The numerical database provides the results from various solvers of several Reynolds-Averaged Navier–Stokes (RANS) turbulent models applied on the wind tunnel configuration and compressible DNS simulations computed on restricted domains embedded in the potential core of the open jet (Wu et al., 2020; Arroyo et al., 2022). Far-field noise has been predicted by applying the FWH analogy as given in Casalino (2003) on the solid surface of the airfoil and on a porous surface enclosing the airfoil. Notably, discrepancies still exist between the two predictions and with experimental results at high frequencies. Furthermore, the validity of approximating the effect of the open jet using a mean flow field has yet to be determined. While previous works using the Lattice Boltzmann Method (LBM) (Sanjose et al., 2014; Moreau et al., 2019; Zhou et al., 2025) have shown that the pressure distribution on the CD airfoil is sensitive to the state of the shear layer in the simulation, its effect on turbulent statistics has not yet been fully examined. According to Caiazzo et al. (2023), displacement thickness, edge velocity and Reynolds stress can serve as scaling parameters of wall-pressure fluctuation intensity on the wall near the airfoil trailing

* Corresponding author.
E-mail address: zhouziyang5@gmail.com (Z. Zhou).

https://doi.org/10.1016/j.ijheatfluidflow.2025.110207
Received 8 August 2025; Received in revised form 9 December 2025; Accepted 12 December 2025
Available online 26 December 2025

Nomenclature

English symbols

APG	Adverse pressure gradient
c	Chord length of the airfoil
C_f	Friction coefficient
c_i	Discretized velocity space
f_i	Discrete-velocity distribution function
t_{TF}	Through flow times
FPG	Favorable pressure gradient
h	Height of the zigzag trip
LE	Leading edge
LSB	Laminar separation bubble
p_{ref}	Reference pressure taken at exit of nozzle
Re_θ	Reynolds number based on momentum thickness
S_{ij}	Strain rate, $S_{ij} = \frac{1}{2}(\frac{du_i}{dx_j} + \frac{du_j}{dx_i})$
TE	Trailing edge
U_∞	Free-stream velocity
U_e	Boundary layer edge velocity
u_τ	Friction velocity
u_τ	Friction velocity
U_{ref}	Reference velocity taken at exit of nozzle
ZPG	Zero pressure gradient

Greek symbols

α	Geometric angle of attack
α_i	Instantaneous angle of attack relative to α
β_C	Clauser parameter, $\beta_C = \delta^*/\tau_w \times d\bar{p}/ds$
δ	Boundary layer thickness
δ^*	Boundary layer displacement thickness
E_{11}	Longitudinal velocity spectrum
γ	Coherence
H	Boundary layer shape factor
p_e	Boundary layer edge pressure
κ	von Kármán constant
μ	Dynamic viscosity
ν	Kinematic viscosity
ω	Angular frequency
θ	Boundary-layer momentum thickness

Abbreviations

DNS	Direct Numerical Simulation
DNS-SLR	DNS with shear layer refinement
DNS-SLRT	DNS with shear layer refinement and trip
ECL	École Centrale de Lyon
PSD	Power Spectral Density
FWH	Ffowcs- William and Hawking
SPL	Sound Pressure Level
VR	Voxel Refinement
MSU	Michigan State University
UdeS	Université de Sherbrooke

edge and therefore can characterize the magnitude of scattered acoustic perturbations. Understanding the influence of installation effects on these parameters can shed light on the mechanism by which the installation influences far field acoustic pressure and guide future efforts to quantify its influence.

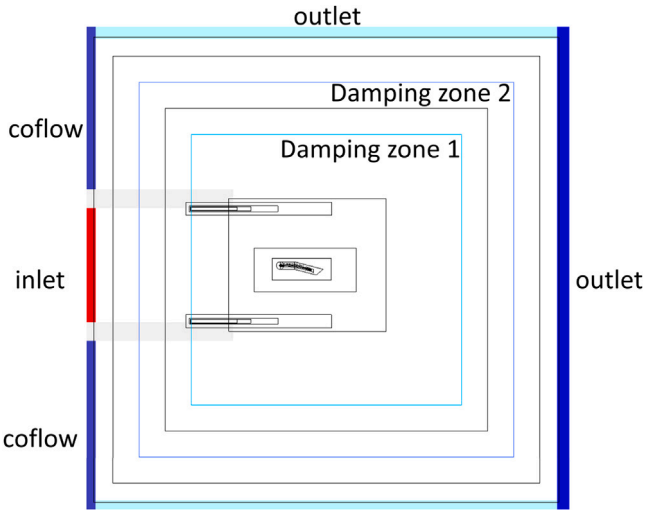

Fig. 1. VR regions used for shear layer refinement. Thin black lines represent VR regions, light blue line represents Damping Zone 1 and dark blue line represents Damping Zone 2. (For interpretation of the references to color in this figure legend, the reader is referred to the web version of this article.)

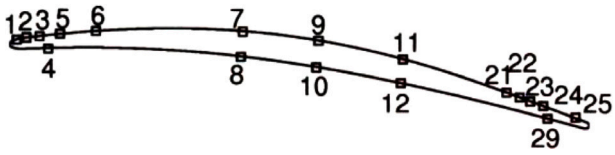

Fig. 2. RMP locations along the airfoil surface.

2. Numerical configuration

2.1. Computational domain

The numerical methodology employed for the simulations of the installed CD airfoil is summarized in this section. This methodology is based upon previous work (Sanjose and Moreau, 2011; Zhou et al., 2025) and emphasis is given on the main specificity of the simulations investigated in the present work.

The computational domain in this simulation, shown in Fig. 1, mimics several open-jet experimental set-ups (Moreau and Roger, 2005; Jaiswal et al., 2020) including that in the anechoic wind tunnel facility at Université de Sherbrooke (UdeS) (Jaiswal et al., 2023). The geometry of the open jet nozzle is included in the computational domain in a simplified manner. This is because accounting for the resultant installation effects is absolutely necessary to reproduce the proper loading on the airfoil and thus the proper turbulent boundary-layer development on the suction side and consequently the noise radiated in the far field (Moreau et al., 2003). The CD airfoil, placed in the potential core of this jet, has a chord length of $c = 0.1356$ m. The angle of attack, defined by the angle between the chord line and the principle axis of the wind tunnel, is 8 degrees. The simulation is limited to a span width of $0.1\,c$ with periodic boundary conditions used in the spanwise direction. This span length has been demonstrated to be sufficient through previous numerical studies by Wu et al. (2020) and Wang et al. (2009) along with experimental study by Moreau and Roger (2005). The inlet velocity is 16 m/s with a coflow of 0.165 m/s. The boundary conditions are defined in Fig. 1. Pressure probes are set on the surface of the airfoil at locations corresponding to the Remote Microphone Probe (RMP) positions in experiments (Moreau and Roger, 2005; Jaiswal et al., 2020) as shown in Fig. 2.

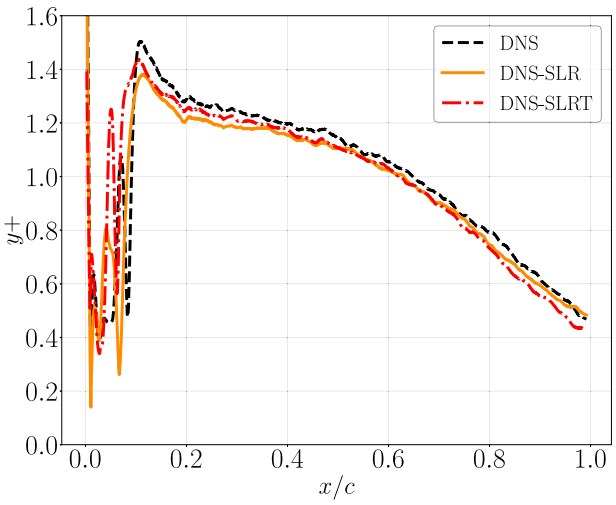

Fig. 3. y^+ on the suction side of the airfoil.

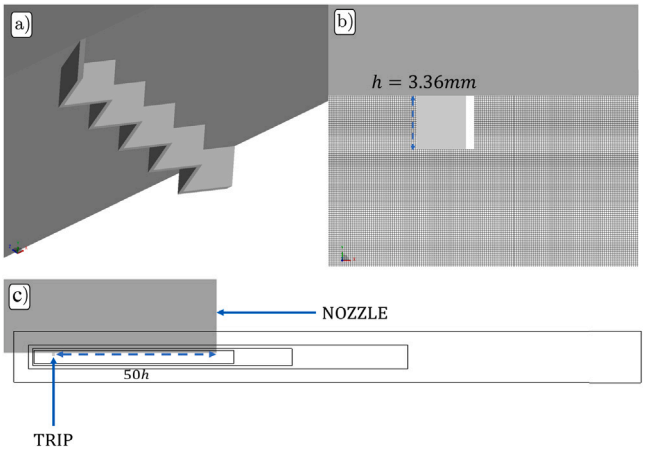

Fig. 4. Geometry and Mesh of Zigzag Trip. (a) Zigzag trip on Upper Lip; (b) Voxel Refinement for Turbulent Trip (Every 2 grid lines shown).; (c) The location of the trip relative to the open jet nozzle.

2.2. Numerical method

In the present study, the LBM is used (He and Luo, 1997; Chen, 1998) with the solver PowerFlow 6.2021.R6. This approach is naturally transient and compressible leading to an insight on hydrodynamics mechanisms responsible for trailing edge (TE) noise sources. In LBM, the Boltzmann equation is solved on a lattice in order to obtain the discrete-velocity distribution function in the multi-dimension phase space, $f_i(\mathbf{x}, t)$, which represents the density of particles with velocity $\mathbf{c}_i = (c_{ix}, c_{iy}, c_{iz})$ at position $\mathbf{x}$ and time t. For the low speed conditions examined in this study, the classical D3Q19 lattice is used, which means that the three dimensional isothermal flow field is solved using 19 directions in-phase space. The classical BGK relaxation model is used for the collision operator. To obtain density ρ and momentum $\rho\mathbf{u}$, weighted sums of f_i are calculated (Krüger et al., 2017):

$$\rho(\mathbf{x}, t) = \sum_i f_i(\mathbf{x}, t) \tag{1}$$

$$\rho\mathbf{u}(\mathbf{x}, t) = \sum_i \mathbf{c_i} f_i(\mathbf{x}, t) \tag{2}$$

2.3. Mesh criteria

The discrete-velocity distribution function is defined in a lattice made up of cubic cells called voxels. The computational domain is then filled with an octree-grid of these voxels with a 1:2 grid refinement (Chen et al., 2006). In order to resolve smaller flow structures, voxel regions (VR) are defined in which the voxel size Δx is specified. 10 voxel regions, shown by the black lines in Fig. 1, are used in the computational domain. The voxel regions are used to impose the required dimensionless y^+ on the surface of the airfoil and to transition into larger cell sizes in areas further away, using the following definitions:

$$y^+ = \frac{y u_\tau}{\nu}, \tag{3}$$

$$u^+ = \frac{u}{u_\tau}. \tag{4}$$

As shown in Fig. 3, $y^+ < 1.5$ is achieved on the airfoil surface (below 1 in the fully turbulent region).

Note also that although the experimental Mach number is 0.05, it has been increased to 0.2 in the simulation. This adjustment is necessary to achieve DNS resolution in the three VR regions closest to the airfoil. To accommodate this Mach number increase, the lattice velocity must be raised, and consequently, lattice viscosity is also increased to maintain a constant Reynolds number. Due to a stability threshold on the relaxation time, the viscosity in VR regions beyond the three finest ones is higher than the specified kinematic viscosity of 1.44×10^{-5} m^2/s. As mentioned in Sanjose and Moreau (2011), the three finest VR regions cover the size of the boundary layer as measured by Neal (2010) in the MSU wind tunnel.

Table 1
CD airfoil studies.

Name	Lip BC	Inlet BC	Trip	Shear layer refinement
DNS-SLR	Slip	Profile	No	Yes
DNS-SLRT	No slip	Uniform	Yes	Yes
DNS	Slip	Profile	No	No
Experiment	N/A	N/A	N/A	N/A

Compared DNS setup (see Table 1), additional voxel refinement regions have been used to capture the development of the turbulent boundary layer downstream of the zigzag trip inside the nozzle resulting in a more turbulent jet shear layer in both the DNS-SLR and the DNS-SLRT cases. In addition, for the DNS-SLRT case 56 voxels are used across the height of the zigzag trip which is $h = 3.36$ mm. Details of the zigzag trip used and the voxel regions in the jet shear layer are given in 4. Using the LBM solver, the simulations shown in Table 1 have been run for 30 through-flow times (t_{TF}), where $t_{TF} = \frac{c}{U_\infty}$. The relevant statistics are then taken from the final 20 through-flow times. Note that the number of through flow times is significantly increased from the previous studies (Wang et al., 2009; Christophe et al., 2009; Sanjose and Moreau, 2011), which only used 5–6 through flow times to gather the turbulent flow statistics around the airfoil. Such a long recording time allows resolution of the low frequency shear layer movements. In total, each case took 129600 CPU-hours on 1440 Intel "Skylake" cores at 2.4 GHz.

3. Results

This section will begin by highlighting the differences in flow features found in the 3 cases, followed by an analysis of the mean velocity and pressure profiles. Wall pressure statistics and far field noise will then ensue.

3.1. Flow topology

Comparing DNS with DNS-SLR results in Fig. 5 reveals significant differences in the topology of the wind tunnel free jet upstream of the airfoil due to refinement. In the original DNS case, the jet shear layer remained laminar up to above the mid chord of the CD airfoil before

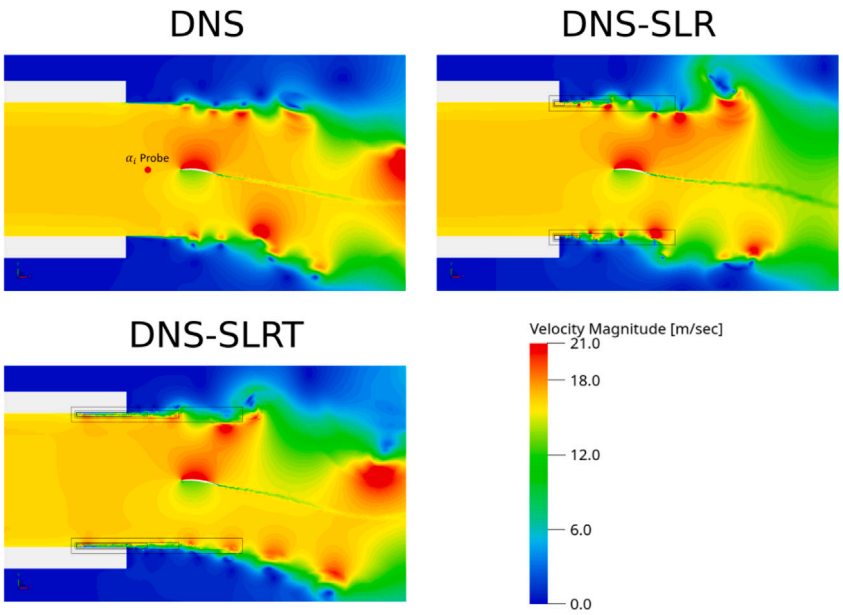

Fig. 5. Mid plane velocity magnitude contours.

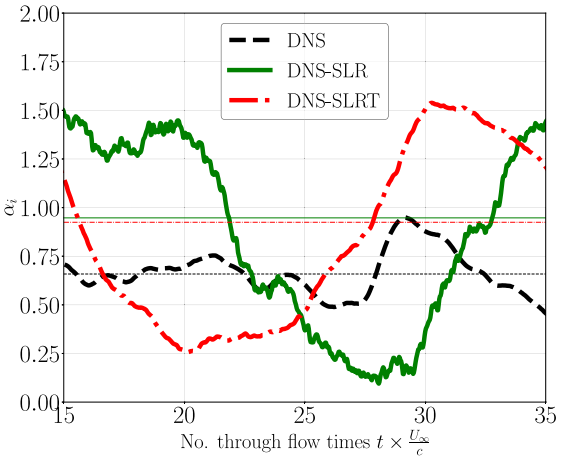

Fig. 6. Correction of angle of attack (α_i). Horizontal straight lines show mean correction of angle of attack ($\overline{\alpha_i}$).

quickly transitioning to turbulence via Kelvin–Helmholtz instabilities and vortex pairing. Conversely, with voxel refinement, the formation of Kelvin–Helmholtz instabilities occurred earlier at the nozzle lip, leading to vortex pairing above the leading edge of the airfoil in the DNS-SLR case that appear enhanced in comparison to the previous case. The introduction of the zigzag trip led to boundary layer transition to turbulence inside the nozzle, mitigating the large instabilities involved in vortex pairing observed in the DNS-SLR case above the leading edge of the airfoil. As a result, vortex pairing occurred further downstream with the addition of the trip.

Due to differences in the development of the jet shear layer, the instantaneous flow angle which is the angle of attack correction ($\alpha_i = \tan^{-1}(U_y/U_x)$) measured 1 chord length upstream of the leading edge (LE), behaves differently in the 3 cases. While α_i is between 0.5° and 1° for 20 through flow times as simulated in the DNS case, in the DNS-SLR and the DNS-SLRT cases the α_i is between 0.0° and 1.5°. Note also that the time-averaged angle-of-attack correction, $\overline{\alpha_i}$, is higher in the DNS-SLR and DNS-SLRT cases than in the DNS case. This will be relevant in the development of the adverse pressure gradient (APG) over the airfoil as shown in the next section.

3.2. Mean pressure coefficient

The mean aerodynamic loading on the airfoil, $\overline{C_p}$ may be observed using the mean pressure coefficient given by

$$\overline{C_p} = \frac{\overline{p} - p_{ref}}{\frac{1}{2}\rho_{ref} U_{ref}^2} \tag{5}$$

where $\overline{p}$ is the mean static pressure at the wall on both suction and pressure sides. p_{ref}, ρ_{ref} and U_{ref} are the reference pressure, density and velocity respectively, taken at the exit of the nozzle. In Fig. 7, good agreement between all numerical and experimental results is seen except in the laminar separation bubble (LSB) identified at $-1.0 < x/c < -0.8$. In particular, the DNS-SLR and DNS-SLRT cases have smaller LSBs than the DNS case. This may be explained not only by the increase in turbulence intensity from 0.3% to 0.5% as mentioned in Zhou et al. (2025), but also by the change in geometrical angle of attack, α_i in Fig. 6. This change in α_i also influences the APG which is quantified by the Clauser parameter $\beta_C = \delta^*/\tau_w \times d\overline{p}/ds$ where δ^* is the boundary-layer displacement thickness and $d\overline{p}/ds$ the gradient of the mean static pressure at the wall in the streamwise direction. As seen in Fig. 8, the Clauser parameter increases more rapidly with respect to the curvilinear abscissa s in the DNS-SLRT and DNS-SLR cases than in the DNS case. Furthermore, the results of Wu et al. (2019) also displayed a sharper increase in β_C than the present DNS case.

3.3. Friction coefficient

In Fig. 9(a), the skin-friction coefficient, given by

$$C_f = \frac{\tau_w}{\frac{1}{2}\rho U_e^2} \tag{6}$$

is plotted against Reynolds number based on momentum thickness, Re_θ. The plot is limited to $x/c > -0.60$ so that only ZPG and APG data is shown. Also shown is the empirical correlation given by Smits et al. (1983). As previously observed by Caiazzo et al. (2023), the C_f over the CD airfoil agrees well with the empirical correlation at the ZPG location. This is represented by $Re_\theta \approx 300$ for Caiazzo et al. (2023) and $Re_\theta \approx 600$ for the DNS, DNS-SLR and DNS-SLRT cases. At higher values of Re_θ, trends of C_f deviates from the empirical correlation as the APG decelerates the boundary layer, increases its thickness and reduces C_f as seen in Vinuesa et al. (2017).

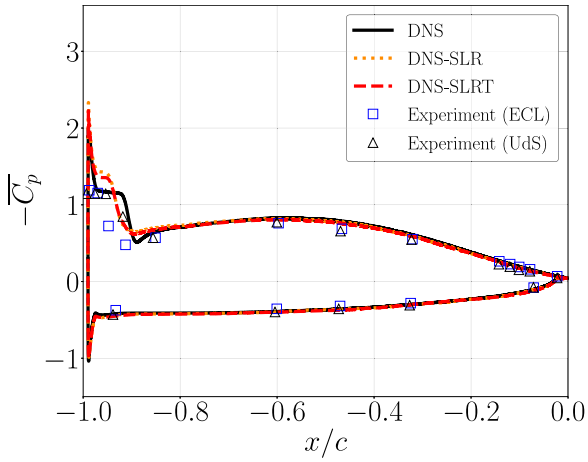

Fig. 7. Mean pressure coefficient.

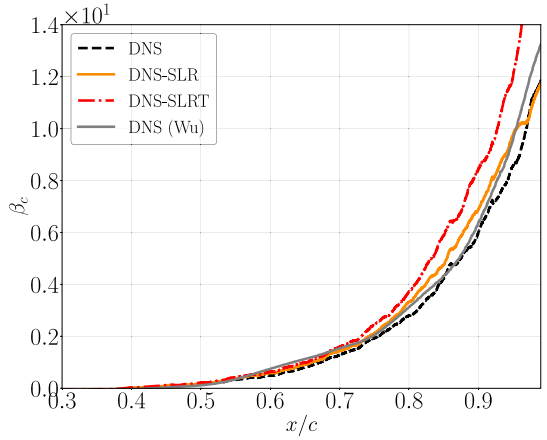

Fig. 8. Clauser parameter, β_c.

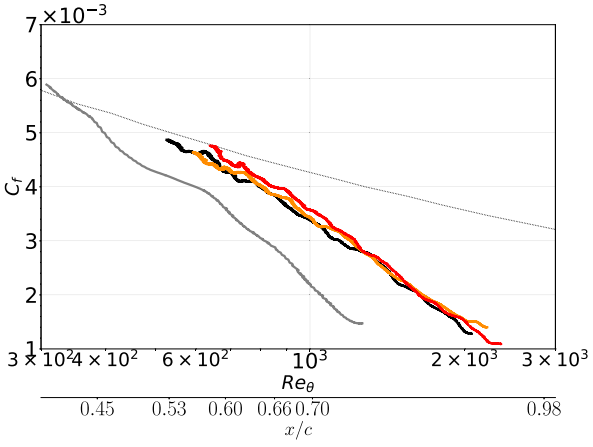

Fig. 9. Friction coefficient, C_f. Secondary x axis below shows corresponding x/c for the DNS case. Dotted line, ···, represent the empirical correlation by Smits et al. (1983). (See Fig. 8 for the legend).

3.4. Mean boundary-layer velocity profiles

To demonstrate the differences in boundary layer development due to differences in conditions, the velocity profiles at 6 locations from the leading edge (LE) to the TE are shown in Fig. 10. Near the LE,

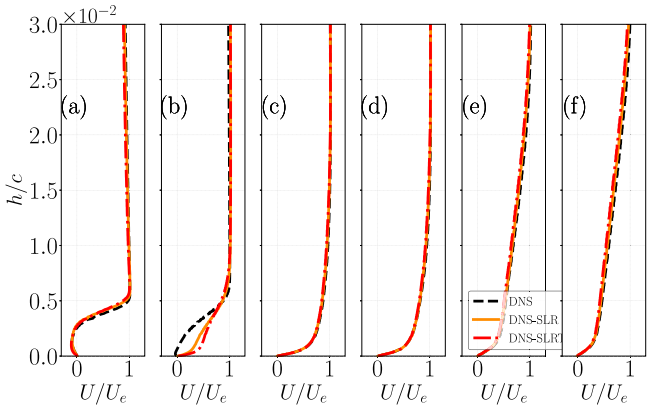

Fig. 10. Boundary layer velocity profile at probes 3, 5, 7, 9, 21 and 24 (from left to right).

Table 2
Properties of the TBL for the current DNS and for several existing studies in the literature.

Case	x/c	Re_θ	β_c	$H = \delta^*/\theta$
DNS, Sensor 7	−0.60	535	−0.018	1.55
DNS-SLR, Sensor 7	−0.60	603	−0.0003	1.52
DNS-SLRT, Sensor 7	−0.60	648	0.01	1.49
DNS, Sensor 9	−0.47	680	0.25	1.56
DNS-SLR, Sensor 9	−0.47	737	0.30	1.53
DNS-SLRT, Sensor 9	−0.47	785	0.33	1.51
DNS, Sensor 21	−0.14	1435	4.39	1.74
DNS-SLR, Sensor 21	−0.14	1533	4.95	1.74
DNS-SLRT, Sensor 21	−0.14	1629	5.71	1.76
DNS, Sensor 24	−0.08	1685	6.97	1.85
DNS-SLR, Sensor 24	−0.08	1814	8.32	1.86
DNS-SLRT, Sensor 24	−0.08	1932	8.92	1.89
Wu et al. (2019), Sensor 7, ZPG	−0.60	319	0.005	1.61
Wu et al. (2019), Sensor 9, ZPG	−0.47	390	0.28	1.61
Wu et al. (2019), Sensor 21, APG	−0.14	877	4.82	1.86
Wu et al. (2019), Sensor 24, APG	−0.08	1036	8.31	2.00
Cohen and Gloerfelt (2018), ZPG	–	1693	0	1.46
Cohen and Gloerfelt (2018), APGw	–	2462	0.41	1.53
Cohen and Gloerfelt (2018), APGs	–	3125	1.41	1.63
Na and Moin (1998), ZPG	0.50/c	586	−0.35	1.41
Na and Moin (1998), APG	0.85/c	1229	1.78	1.54
Spalart (1988), ZPG	–	300	–	1.66

the DNS case contains a LSB that extends up to probe 5 while the transition to turbulence has already occurred at this location in the DNS-SLR and DNS-SLRT cases. In the zero pressure gradient (ZPG) region at probes 7 and 9, the 3 cases have similar thicknesses at mid-chord but the thickness deviates at the trailing edge at probes 21 and 24. Similarly, as shown in Fig. 11(a) to (c), the DNS-SLR and DNS-SLRT cases show larger δ^* and boundary layer thickness based on 95% of total pressure (δ_{95}) than the DNS case at the TE. This is most likely caused by the differences in $\overline{\alpha_i}$ which increased the APG effects in both these cases. In addition, at $x/c = 0.1$, the shape factor for the DNS case is higher than both DNS-SLR and DNS-SLRT which is a consequence of a longer separation bubble. Despite this difference, the 3 cases show similar shape factors in $0.2 < x/c < 1.0$ to within 3% as seen in Fig. 11(d). Note also that all 3 simulations produced lower thicknesses than in Caiazzo et al. (2023). This is due to a combination of the lower initial thickness after flow reattachment and higher Re_θ in comparison to the DNS in Caiazzo et al. (2023). In order to further quantify the differences in TBL properties at the four sensor locations where the flow is attached, the boundary-layer parameters are listed in Table 2. Additional references by Wu et al. (2020), Na and Moin (1998) and Spalart (1988) have also been included to provide further datasets for comparison.

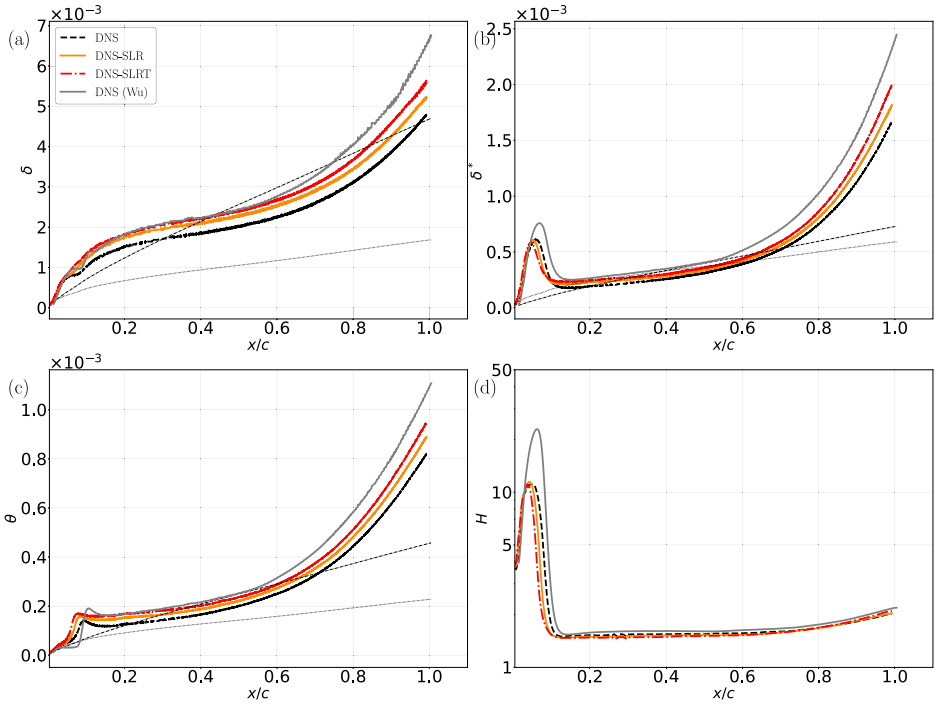

Fig. 11. Boundary layer parameters at attached flow locations. Results from Schlichting et al. (2017) ··· laminar flat plate; and ––, turbulent flat plate.

To analyze the viscous sub-layer and the log layer spread inside the boundary layer, the streamwise velocity profiles, normalized by inner variables (y^+ and u^+), are shown in Fig. 12. The von Kármán constant κ (Von Kármán, 1931) and the constant B are taken from Wu et al. (2019). $\kappa = 0.41$ and $B = 4.5$ are used for the ZPG cases and $\kappa = 0.30$ and $B = -1.38$ for the APG cases. The present results are then compared to the DNS results of Wu et al. (2019) (grey line) along with the numerical datasets of Spalart (1988), Na and Moin (1998) and Cohen and Gloerfelt (2018) (all symbols). While the former is an airfoil simulation, the three latter cases are channel flows with pressure gradients imposed using the appropriate boundary conditions. The boundary layer parameters are given in Table 2. All positions show a clear development of a turbulent boundary layer (TBL) on the airfoil suction side. At the 2 ZPG locations (sensors 7 and 9), excellent agreement is found between the present results and the other DNS. The longer log layers from the other datasets can be explained by the higher Re_θ, which causes wider length-scale separation between the smallest and largest eddies as described in Spalart (1988). At the two APG locations (sensors 21 and 24), all results show a steeper slope in the log region than at the ZPG locations due to pressure gradient effects (Caiazzo et al., 2023).

The slightly stronger wake region of the velocity profile at probe 24 in the results of Wu et al. (2019) is likely because the higher Re_θ in the 3 DNS causes values of U^+ in the boundary layer to be less sensitive than in Wu et al. (2019). Note that this trend was also reported by Vinuesa et al. (2018). The former case is actually close to flow separation as highlighted by the separated TBL case (blue squares) taken from Na and Moin (1998).

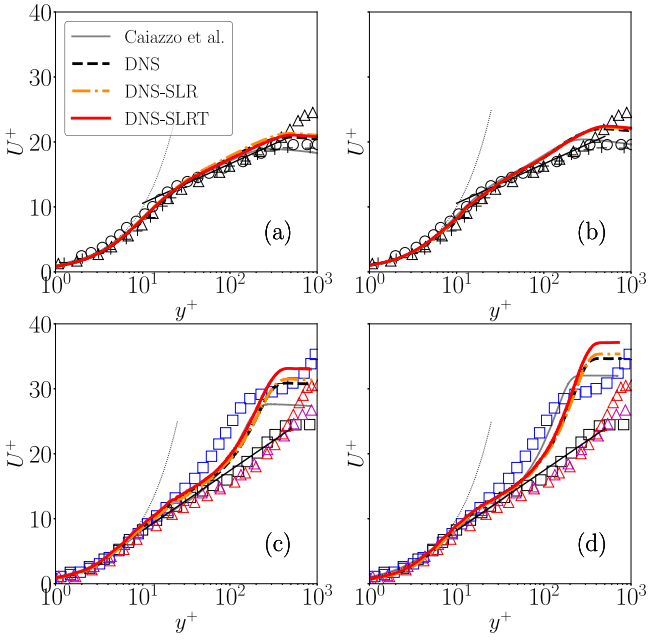

Fig. 12. Streamwise velocity profiles at probes: (a) 7, (b) 9, (c) 21, (d) 24. Symbols: + ZPG ($Re_\theta = 300$), Spalart (1988); ∘ ZPG ($Re_\theta = 586$), □ APG ($Re_\theta = 1229$), □ Separated TBL (Na and Moin, 1998); △ ZPG ($Re_\theta = 1693$), △ APGs ($Re_\theta = 3125$), △ APGw ($Re_\theta = 2462$) (Cohen and Gloerfelt, 2018); ···, $u^+ = y^+$; –, $u^+ = (1/\kappa)\ln(y^+) + B$.

3.5. Reynolds stress tensor

The normalized Reynolds stress components, u_{rms}, v_{rms}, $\overline{uv}$, are normalized with inner variables as $u_{rms} = u^+_{rms}/u_\tau$, $v_{rms} = v^+_{rms}/u_\tau$ and $\overline{uv}^+ = \overline{uv}/u^2_\tau$. They are shown in Figs. 13 to 15.

The root-mean-square velocity profiles, u_{rms} (streamwise) and v_{rms} (wall-normal), are presented for different probe locations. At probes 7 and 9, the profiles are shown with ZPG results, while at probes 21 and 24, they are shown with APG results. Both the ZPG and APG data are sourced from studies by Cohen and Gloerfelt (2018), Na and Moin (1998), and Spalart (1988). As the flow progresses from probe 7 to probe 24, it encounters APG effects, causing the peak values of u_{rms} and v_{rms} to spread and shift farther away from the wall.

The current DNS, DNS-SLR and DNS-SLRT results show u_{rms} and v_{rms} that appear shifted further upwards than the results of Caiazzo et al. (2023) because they were obtained at higher Re_θ. Despite the

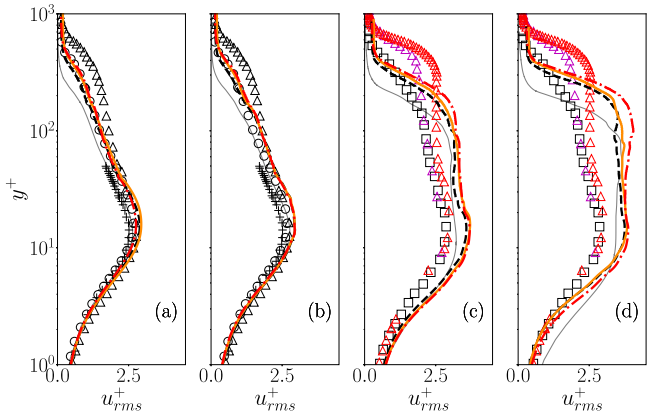

Fig. 13. u^+_{rms} at sensors (a) 7, (b) 9, (c) 21 and (d) 24. Refer to Fig. 12 for labels.

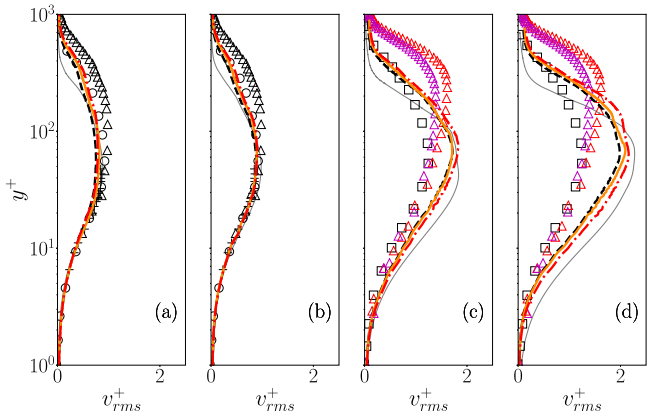

Fig. 14. v^+_{rms} at sensors (a) 7, (b) 9, (c) 21 and (d) 24. Refer to Fig. 12 for labels.

agreement between DNS, DNS-SLR and DNS-SLRT results for u_{rms} and v_{rms} at the ZPG probes, a slightly higher outer peak of u_{rms} sets the DNS-SLRT apart at probe 24. This is likely due to the effect of stronger β_C (as evidenced in Fig. 8) which causes an increase in large-scale eddies in outer region (Bradshaw, 1967).

In addition, uv^+, shown in Fig. 15, is an important parameter for the scaling of wall-pressure statistics as demonstrated by Caiazzo et al. (2023). At probe 7 in the ZPG region, uv^+ matches well with flat plate DNS results by Spalart (1988). As the trailing edge is approached, all DNS results deviate from flat plate results due to the influence of the adverse pressure gradient as mentioned by Caiazzo et al. (2023). On the other hand, the DNS, DNS-SLR and DNS-SLRT results show higher uv^+ in the outer layer than in Caiazzo et al. (2023) and this is likely a result of higher Re_θ, according to Rkein and Laval (2023).

To demonstrate the similarity of Reynolds stress profiles under different boundary layer conditions, the mixed scaling proposed by Han et al. (2024) is used to collapse the $\overline{uv}$ data from the present DNS and that of Caiazzo et al. (2023) and is defined as:

$$\overline{uv}_{apg} = U_e^2 \frac{\delta^*}{\delta}\left(1 + H\frac{\delta}{\rho U_e^2}\frac{dP_e}{dx}\right). \tag{7}$$

As seen in Fig. 16 where uv^+, U_{zs} and uv_{apg} are used to scale the profile of $\overline{uv}$, superior collapse is given by the mixed scaling. This shows that the peak $\overline{uv}$ is more effectively scaled using mixed scaling than with either inner or outer scaling.

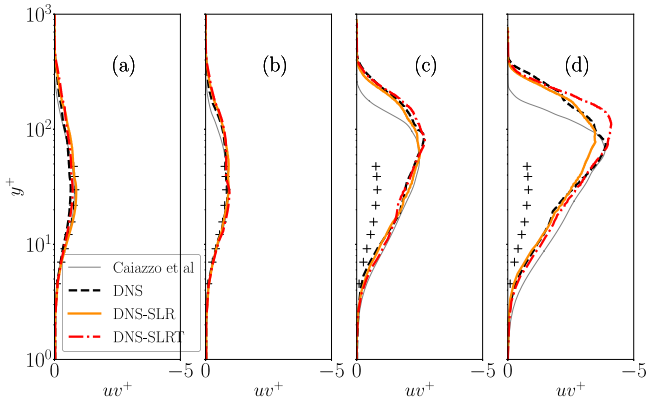

Fig. 15. uv^+ at probes (a) 7, (b) 9, (c) 21 and (d) 24.

3.6. Velocity spectra

Before analyzing the wall-pressure statistics, it is worth analyzing the velocity spectrum to reveal if DNS resolution has been actually achieved in the boundary layer. This is done by plotting the one-dimensional streamwise velocity spectrum E_{11} in the DNS case. The Kolmogorov scale η represents the smallest length scale of eddies in turbulent flow and is defined by $\eta = (\upsilon^3/\varepsilon)^{1/4}$ where $\varepsilon = 2\nu\overline{S_{ij}S_{ij}}$ is the dissipation rate and the strain rate is given by $S_{ij} = \frac{1}{2}(\frac{\partial u_i}{\partial x_j} + \frac{\partial u_j}{\partial x_i})$. Here, frozen turbulence was assumed (Taylor, 1938), which implies the streamwise wavenumber k_1 to be proportional to the frequency f as:

$$k_1 = \frac{2\pi f}{\overline{U}}, \tag{8}$$

with $\overline{U}$ the local mean velocity. Fig. 17 shows the normalized E_{11} at 4 locations in the boundary layer above probe 7 and probe 24 (see Fig. 2 for locations). Probe 24 monitors DNS resolution near the trailing edge, while probe 7 checks for proper resolution further upstream. As shown by the dotted lines in both figures, DNS resolution has been achieved at both locations. Similar results are expected for the DNS-SLR and DNS-SLRT cases.

3.7. Wall-pressure spectra

The power spectral density (PSD) of the 3 cases at probe 3 to probe 24 on the suction side of the airfoil are shown in Fig. 18 for the 3 cases. The experimental results captured at UdeS and ECL are also included. At probe 3, the DNS case show lower spectral levels than the DNS-SLR and DNS-SLRT cases due to the probe being inside the LSB whereas the LSB begins to reattach at this location in the DNS-SLR and DNS-SLRT cases. At probe 5, an increase in spectral levels and a weaker broadband hump are seen for all the numerical cases. Downstream of the LSB reattachment (probe 7 to probe 24), there is an overall good agreement between numerical simulation and the UdeS experimental results. The wall PSD levels between the 3 DNS cases are also similar.

3.8. Coherence length

In addition to wall pressure spectra, the coherence length of pressure fluctuations under the turbulent boundary layer as it passes over the trailing edge is also acoustically relevant is thus of interest for a study of installation effects from an acoustics standpoint. Coherence, denoted γ^2, is defined by

$$\gamma^2(f,\Delta z) = \frac{\left|\Phi_{p'p'}(f,\Delta z)\right|^2}{\Phi_{p'p'}(f,0)\,\Phi_{p'p'}(f,0)}, \tag{9}$$

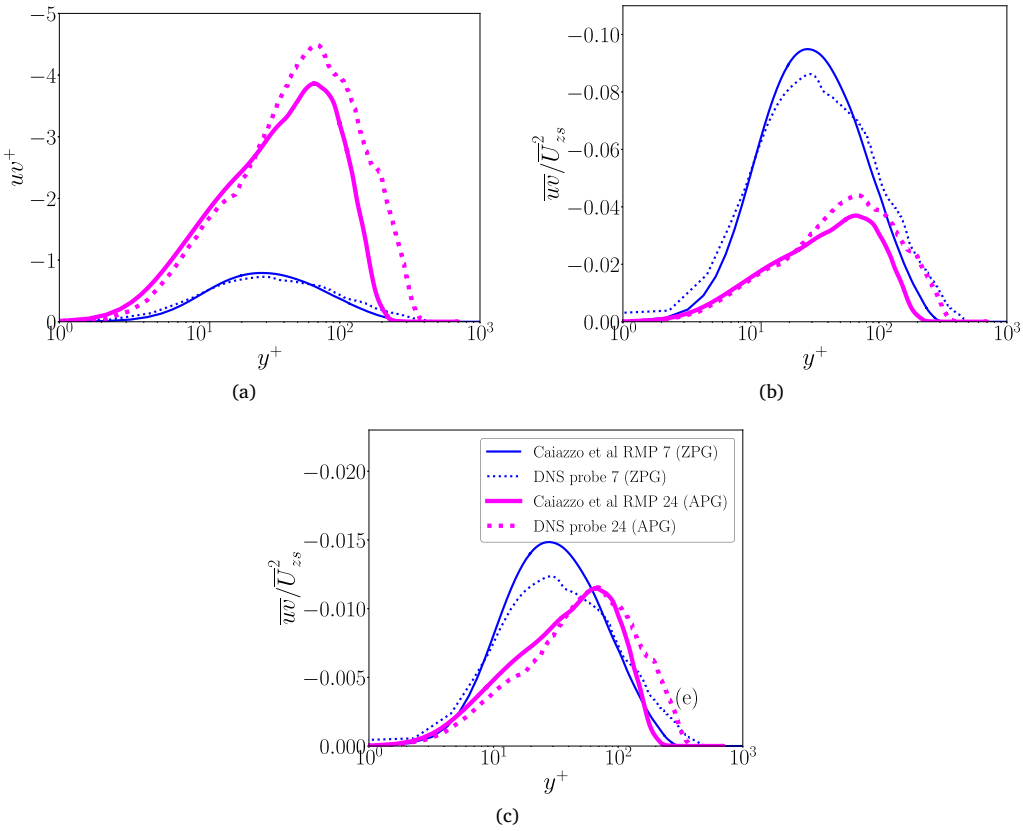

Fig. 16. Reynolds stress with (a) inner, (b) outer scaling and (c) mixed scaling.

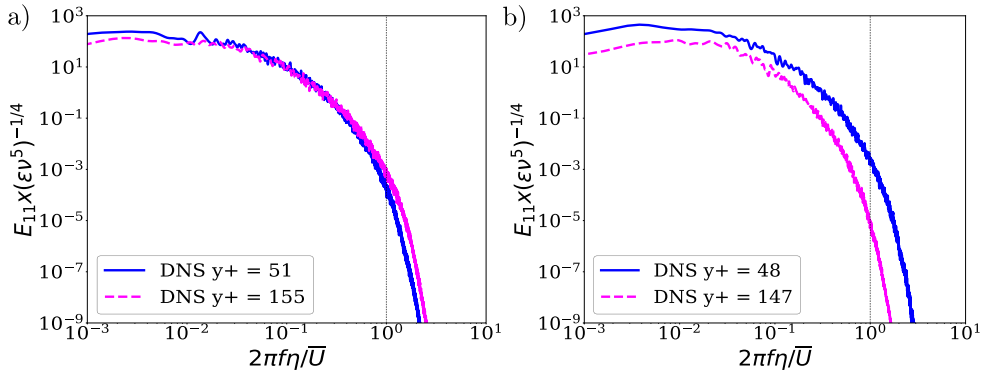

Fig. 17. Normalized streamwise velocity spectra: (a) Probe 7; (b) Probe 24.

where $\gamma^2(f,\Delta z)$ is the cross spectral density of p' at two locations at a given chordwise location with a spanwise spacing of Δz. Furthermore, the coherence length, l_s, is defined by

$$l_s(f) = \int_0^\infty \gamma^2(f,\Delta z)\,\mathrm{d}\Delta z, \tag{10}$$

which is the integration of the coherence γ^2 across the spanwise direction at a given chordwise location. Fig. 19 shows that l_s remains nearly unchanged between RMP 7 and RMP 24 in the frequency range of interest. This confirms that the spatial coherence of the pressure fluctuations sees little influence of installation effects.

3.9. Farfield noise

PSD of the far-field acoustic pressure are obtained using the Ffowcs-William and Hawking (FWH) analogy applied to the airfoil surface. The FWH analogy is used because it accounts for the surface dipoles caused by TE scattering which is the subject of this study. These results are compared with the measurements achieved at UdeS and ECL. The latter was taken at 2 m from the airfoil trailing edge and at 90° above the suction side and is represented by the black line in Fig. 20. As detailed in Zhou et al. (2025), the stronger vortex pairing in the jet shear layer of the DNS-SLR case seen in Fig. 5 results in low frequency pressure footprints on the airfoil and causes additional low frequency noise below 1000 Hz. In the mid frequency range (1000 Hz to 5000 Hz), Wu et al. (2020) showed that the filtered dilatation field was dominated by a pure trailing-edge noise contribution. In this frequency range, good agreement exists between all the DNS results, suggesting that the differences in the aforementioned boundary layer statistics do not make a significant difference to the pure TE noise contribution. At higher frequencies, the DNS-SLR and DNS-SLRT cases show the presence of a high frequency hump at 5000 Hz. This latter was shown by Zhou et al.

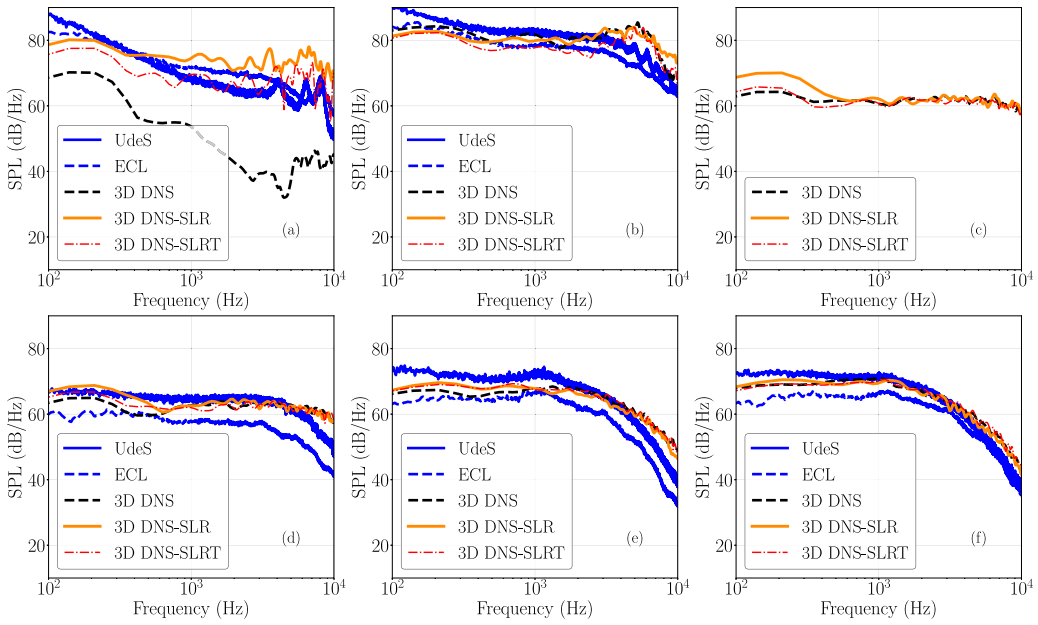

Fig. 18. Wall-pressure spectra on airfoil suction side. Sensors (a) 3, (b) 5, (c) 7, (d) 9, (e) 21, (f) 24.

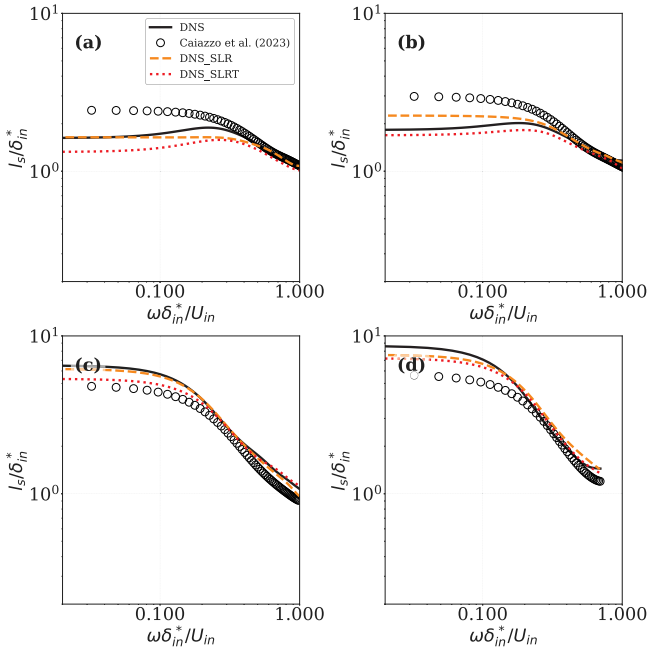

Fig. 19. Spanwise coherence length l_s on airfoil suction side normalized by boundary layer thickness at RMP 7 δ_{in}. Sensors (a) 7, (b) 9, (c) 21, (d) 24.

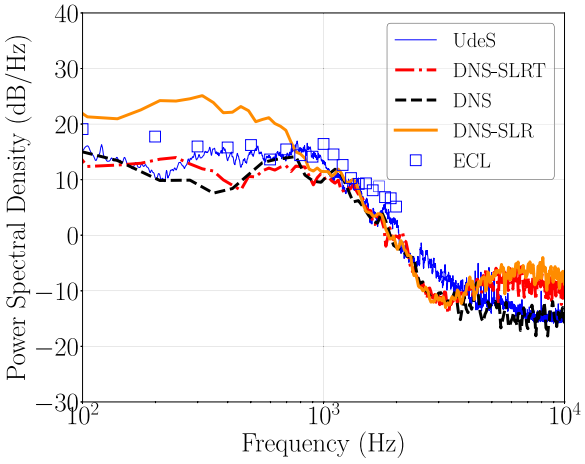

Fig. 20. Farfield noise computed using SherFWH.

(2025) to be coming from the LSB reattachment near the LE. It is not present in the DNS case because there is less LSB activity and lower fluctuations in α_i as identified in Fig. 6.

4. Conclusion

Three DNS simulations of the flow over a controlled-diffusion airfoil at a chord-based Reynolds number of 1.5×10^5, a Mach number of 0.2 and a 8° geometrical angle-of-attack have been achieved with Lattice Boltzmann Method (LBM) as implemented in PowerFLOW. The configuration is of an airfoil installed in a typical open-jet wind tunnel set-up and aims to assess the effect of the jet state on the airfoil aerodynamics and emitted noise for the first time. The three DNS setups differ by additional voxel refinement in the wind tunnel shear layer for DNS-SLR, and by the addition of a turbulent trip to trigger transition in DNS-SLRT. Additional APG effects caused by a slight increase in $\overline{\alpha_i}$ in the DNS-SLR and DNS-SLRT cases over the DNS case caused a thicker laminar separation bubble at the LE and the boundary layer to thicken towards the trailing-edge (TE). Clauser's parameter β_c also increased more rapidly in the DNS-SLRT and DNS-SLR cases after mid-chord. As a consequence, a slight offset away from the wall was seen for uu^+, vv^+ and uv^+ in the DNS-SLRT case. However, peak uv^+ changed by less than 6% even at the TE.

The present work also confirmed that the mixed scaling proposed by Han et al. (2024) gives a better collapse of $\overline{uv}$ than both inner scaling and outer scaling. Finally, despite the initial boundary layer development shifts associated to the angle of attack fluctuations, the turbulence statistics differences did not result in substantial differences in wall pressure fluctuation spectra downstream of the mid chord. Furthermore, spatial correlations computed for the first time on the suction side also remained consistent as demonstrated by the spanwise correlation length which remained unchanged. As a result, the far-field

noise levels in the mid frequency range (1000 Hz to 5000 Hz), where TE noise is the dominant source, were not modified between the three DNS setups. Note that at other frequencies, the modification of the main secondary noise source, the LSB, alters the far-field acoustic spectra, which means that in regimes where the latter becomes dominant, either at high Mach numbers (Deuse and Sandberg, 2020; Shubham et al., 2022) or at high angle of attack (Zhou et al., 2024) for instance, the jet status needs to be accounted for properly and should be carefully checked in experiments.

TE noise predictions often rely on RANS informed turbulence statistics to compute far-field noise using Amiet's approach (Lee et al., 2021). The present findings suggest that the TE noise is not sensitive to cross-velocity correlation within the wind tunnel jet shear layer and that RANS turbulence closure assuming isotropic turbulence are sufficient for this task. Finally, this study shows that far-field noise differences from changes in the wind tunnel shear layer are mainly due to secondary sources from the vortex pairing and the airfoil LSB. These effects overshadow the differences caused by the contribution of trailing edge noise.

CRediT authorship contribution statement

Ziyang Zhou: Writing – review & editing, Writing – original draft, Visualization, Validation, Methodology, Investigation, Formal analysis, Conceptualization. **Stéphane Moreau:** Writing – review & editing, Supervision, Resources, Methodology, Funding acquisition, Conceptualization. **Marlène Sanjosé:** Writing – review & editing, Supervision, Resources, Methodology, Conceptualization.

Declaration of competing interest

The authors declare that they have no known competing financial interests or personal relationships that could have appeared to influence the work reported in this paper.

Acknowledgments

The authors acknowledge Calcul Quebec and Digital Research Alliance of Canada for providing the necessary computational resources for this work, and Dassault Systems for providing the Powerflow licenses and support. They also acknowledge the support of the Natural Sciences and Engineering Research Council of Canada (NSERC) through the Discovery grant.

Data availability

Data will be made available on request.

References

Arroyo, Andrea, Moreau, Stéphane, Sandberg, Richard D., Bauerheim, Michaël, Jacob, Marc C., 2022. Direct numerical simulation of controlled diffusion airfoil self-noise. In: 28th AIAA/CEAS Aeroacoustics 2022 Conference. p. 2815.

Bradshaw, Peter, 1967. The turbulence structure of equilibrium boundary layers. J. Fluid Mech. 29 (4), 625–645.

Caiazzo, A., Pargal, S., Wu, H., Sanjosé, M., Yuan, J., Moreau, S, 2023. On the effect of adverse pressure gradients on wall-pressure statistics in a controlled-diffusion aerofoil turbulent boundary layer. J. Fluid Mech. 960, A17.

Casalino, Damiano, 2003. An advanced time approach for acoustic analogy predictions. J. Sound Vib. 261 (4), 583–612.

Chen, H., 1998. Volumetric formulation of the lattice Boltzmann method for fluid dynamics: Basic concept. Phys. Rev. E 58 (3), 3955–3963.

Chen, Hudong, Filippova, Olga, Hoch, James, Molvig, Kim, Shock, Rick, Teixeira, Chris, Zhang, Raoyang, 2006. Grid refinement in lattice Boltzmann methods based on volumetric formulation. Phys. A 362 (1), 158–167.

Christophe, Julien, Anthoine, Jérome, Moreau, Stéphane, 2009. Trailing edge noise of a controlled-diffusion airfoil at moderate and high angle of attack. In: 15th AIAA/CEAS Aeroacoustics Conference (30th AIAA Aeroacoustics Conference). p. 3196.

Cohen, Elie, Gloerfelt, Xavier, 2018. Influence of pressure gradients on wall pressure beneath a turbulent boundary layer. J. Fluid Mech. 838, 715–758.

Deuse, Mathieu, Sandberg, Richard D., 2020. Different noise generation mechanisms of a controlled diffusion aerofoil and their dependence on Mach number. J. Sound Vib. 476, 115317.

Han, Mingze, Ma, Mingze, Yan, Chao, 2024. Consistent outer scaling and analysis of adverse pressure gradient turbulent boundary layers. J. Fluid Mech. 982, A17.

He, X., Luo, L.-S., 1997. Theory of the Lattice-Boltzmann method: From the Boltzmann equation to the lattice Boltzmann equation. Phys. Rev. E 56 (6), 6811–6817.

Jaiswal, Prateek, Moreau, Stéphane, Avallone, Francesco, Ragni, Daniele, Pröbsting, Stefan, 2020. On the use of two-point velocity correlation in wall-pressure models for turbulent flow past a trailing edge under adverse pressure gradient. Phys. Fluids 32 (10), 105105.

Jaiswal, Prateek, Rendón, Jose, Moreau, Stéphane, 2023. Aeroacoustic investigation of airfoil at near-stall conditions. Phys. Fluids 35 (9).

Krüger, Timm, Kusumaatmaja, Halim, Kuzmin, Alexandr, Shardt, Orest, Silva, Goncalo, Viggen, Erlend Magnus, 2017. The Lattice Boltzmann method. Springer Int. Publ. 10 (978–3), 4–15.

Lee, Seongkyu, Ayton, Lorna, Bertagnolio, Franck, Moreau, Stephane, Chong, Tze Pei, Joseph, Phillip, 2021. Turbulent boundary layer trailing-edge noise: Theory, computation, experiment, and application. Prog. Aerosp. Sci. 126, 100737.

Moreau, Stéphane, Henner, Manuel, Iaccarino, Gianluca, Wang, Meng, Roger, Michel, 2003. Analysis of flow conditions in freejet experiments for studying airfoil self-noise. AIAA J. 41 (10), 1895–1905.

Moreau, S., Neal, D., Foss, J., 2006. Hot-wire measurements around a controlled diffusion airfoil in an open-jet anechoic wind tunnel. J. Fluids Eng. 128 (4), 699–706.

Moreau, S., Roger, M., 2005. Effect of airfoil aerodynamic loading on trailing-edge noise sources. AIAA J. 43 (1), 41–52.

Moreau, Stéphane, Sanjosé, Marlène, Lyu, Benshuai, Ayton, Lorna J, 2019. Analytical, numerical and experimental investigation of trailing-edge noise reduction on a controlled diffusion airfoil with serrations. In: 25th AIAA/CEAS Aeroacoustics Conference. p. 2450.

Na, Y., Moin, Parviz, 1998. The structure of wall-pressure fluctuations in turbulent boundary layers with adverse pressure gradient and separation. J. Fluid Mech. 377, 347–373.

Neal, Douglas R., 2010. The Effects of Rotation on the Flow Field Over a Controlled-Diffusion Airfoil. Michigan State University.

Rkein, Hussein, Laval, Jean-Philippe, 2023. Direct numerical simulation of adverse pressure gradient turbulent boundary layer up to Re_θ=8000. Int. J. Heat Fluid Flow 103, 109195.

Roger, M., Moreau, S., 2004. Broadband self noise from loaded fan blades. AIAA J. 42 (3), 536–544.

Sanjose, Marlene, Méon, Claire, Moreau, Stephane, Idier, Alexandre, Laffay, Paul, 2014. Direct numerical simulation of acoustic reduction using serrated trailing-edge on an isolated airfoil. In: 20th AIAA/CEAS Aeroacoustics Conference. p. 2324.

Sanjose, M., Moreau, S., 2011. Direct numerical simulation of self-noise of an installed control-diffusion airfoil. Can. Acoust. 39 (3), 30–31.

Schlichting, Hermann, Gersten, Klaus, Schlichting, Hermann, Gersten, Klaus, 2017. Boundary–layer equations in plane flow; plate boundary layer. In: Boundary-Layer Theory. Springer, pp. 145–164.

Shubham, S., Sandberg, R., Moreau, S., Wu, H., 2022. Surface pressure spectrum variation with Mach number on a CD airfoil. J. Sound Vib. 526, 116762:1–15.

Smits, A.J., Matheson, N., Joubert, P.N., 1983. Low-Reynolds-number turbulent boundary layers in zero and favorable pressure gradients. J. Ship Res. 27 (03), 147–157.

Spalart, Philippe R., 1988. Direct simulation of a turbulent boundary layer up to Rθ=1410. J. Fluid Mech. 187, 61–98.

Taylor, Geoffrey Ingram, 1938. The spectrum of turbulence. Proc. R. Soc. Lond. Ser. A-Math. Phys. Sci. 164 (919), 476–490.

Vinuesa, Ricardo, Hosseini, Seyed M, Hanifi, Ardeshir, Henningson, Dan S, Schlatter, Philipp, 2017. Pressure-gradient turbulent boundary layers developing around a wing section. Flow Turbul. Combust. 99, 613–641.

Vinuesa, Ricardo, Negi, Prabal Singh, Atzori, Marco, Hanifi, Ardeshir, Henningson, Dan S, Schlatter, Philipp, 2018. Turbulent boundary layers around wing sections up to Rec=1,000,000. Int. J. Heat Fluid Flow 72, 86–99.

Von Kármán, Theodore, 1931. Mechanical Similitude and Turbulence. National Advisory Committee for Aeronautics.

Wang, Meng, Moreau, Stephane, Iaccarino, Gianluca, Roger, Michel, 2009. LES prediction of wall-pressure fluctuations and noise of a low-speed airfoil. Int. J. Aeroacoustics 8 (3), 177–197.

Wu, H., Moreau, S., Sandberg, R.D., 2019. Effects of pressure gradient on the evolution of velocity-gradient tensor invariant dynamics on a controlled-diffusion aerofoil at. J. Fluid Mech. 868, 584–610.

Wu, Hao, Moreau, Stéphane, Sandberg, Richard D., 2020. On the noise generated by a controlled-diffusion aerofoil at Rec= 1.5×10^5. J. Sound Vib. 487, 115620.

Zhou, Ziyang, Moreau, Stephane, Sanjosé, Marlène, 2024. On the noise mechanisms of a controlled diffusion airfoil at high angle-of-attack. In: 30th AIAA/CEAS Aeroacoustics Conference, Rome, Italy.

Zhou, Ziyang, Moreau, Stéphane, Sanjosé, Marlène, 2025. Installation effects on airfoil self-noise estimated by direct numerical simulations. J. Sound Vib. 604, 118978.